Biochemical Studies Provide Insights into the Necessity for Multiple *Arabidopsis thaliana* Protein-Only RNase P Isoenzymes

Tien-Hao Chen [1,2], Marcos Sotomayor [1] and Venkat Gopalan [1,2]

*1 - **Department of Chemistry and Biochemistry,** The Ohio State University, Columbus, OH 43210, USA*
*2 - **Center for RNA Biology,** The Ohio State University, Columbus, OH 43210, USA*

***Correspondence to Venkat Gopalan:** Department of Chemistry and Biochemistry, The Ohio State University, Columbus, OH 43210, USA. gopalan.5@osu.edu*
https://doi.org/10.1016/j.jmb.2018.11.004
Edited by Philip C Bevilacqua

Abstract

RNase P catalyzes removal of the 5′ leader from precursor tRNAs (pre-tRNAs) in all three domains of life. Some eukaryotic cells contain multiple forms of the protein-only RNase P (PRORP) variant, prompting efforts to unravel this seeming redundancy. Previous studies concluded that there were only modest differences in the processing of typical pre-tRNAs by the three isoforms in *Arabidopsis thaliana* [*At*PRORP1 (organellar), *At*PRORP2 and *At*PRORP3 (nuclear)]. Here, we investigated if different physical attributes of the three isoforms might engender payoffs under specific conditions. Our temperature–activity profiling studies revealed that *At*PRORPs display substrate-identity dependent behavior at elevated temperatures (37–45 °C), with the organellar variant outperforming the nuclear counterparts. Echoing these findings, molecular dynamics simulations revealed that *At*PRORP2 relative to *At*PRORP1 samples a wider conformational ensemble that deviates from the crystal structure. Results from our biochemical studies and molecular dynamics simulations support the idea that *At*PRORPs have overlapping but not necessarily redundant attributes and inspire new perspectives on the suitability of each variant to perform its function(s) in a specific cellular locale.

Introduction

Transfer RNA (tRNA) primary transcripts undergo multiple maturation steps including trimming of the 5′-leader and the 3′-trailer, base modifications, and splicing of introns (when present). RNase P, an essential endonuclease, catalyzes the Mg^{2+}-dependent removal of 5′ leaders [1] and exhibits remarkable diversity in its composition: a catalytic RNA-based ribonucleoprotein (RNP) contains 1 to 10 protein subunits depending on the organism [2–5]; an RNA-free, protein-only variant active even as a single protein is also found in all three domains of life [6,7]. Sequence and structural analyses show that these two types of RNase P, which utilize two distinct macromolecular active-site scaffolds, evolved independently [8–11].

Protein-based RNase P, the focus of this study, falls into two broad classes: HARP (*H*omologs of A*quifex RN*ase *P*), a ~23-kDa protein found thus far in bacteria and archaea [7], and PRORP (*PR*otein-*O*nly *R*Nase *P*), a ~60-kDa protein present in four of the five eukaryal supergroups (Amoebozoa being the exception) [12]. Single-polypeptide recombinant HARPs from bacteria/archaea and PRORPs from algae, plants, and protists cleave a variety of pre-tRNA and non-tRNA substrates *in vitro* [7,13–18]. In *Arabidopsis thaliana* (*At*), a dicot plant, three PRORP isoenzymes are present: *At*PRORP1, *At*PRORP2, and *At*PRORP3 [13]. Here, we examine possible reasons for this intriguing and seeming redundancy.

*At*PRORP1 resides in mitochondria and chloroplasts, while *At*PRORP2 and *At*PRORP3 are localized to the nucleus [13]. Genetic studies showed that *At*PRORP1 is essential for plant viability, and that *At*PRORP2 and *At*PRORP3 are functionally redundant given that single knock-out plants are viable in contrast to double knock-outs [16]. These results are consistent with the sequence relatedness of the three PRORPs. Based on their sequences, spermatophyta (seed-producing plants) PRORPs are grouped into three clusters: organellar PRORPs in clusters I and II,

and nuclear PRORPs in cluster III [12]. Nuclear *At*PRORP2 and *At*PRORP3 share 80% sequence identity and have diverged from organellar *At*PRORP1 (e.g., *At*PRORP1 and *At*PRORP2 share ~48% identity) [19]. The robust activity of all three recombinant *At*PRORPs *in vitro* has enabled structure–function relationship studies, which were undertaken with the intent to account for the presence of three isoenzymes in a single organism.

Crystal structures of *At*PRORP1, *At*PRORP2, and truncated (inactive) human PRORPs reveal a strikingly similar V-shaped architecture comprising three domains: an N-terminal *p*entatrico*p*eptide *r*epeat (PPR) domain, a *c*entral bipartite *z*inc-binding (CZ) domain, and a PIN-like *m*etallo*n*uclease (MN) C-terminal domain (Fig. S1) [10,20–23]. PPR proteins are mainly found in eukarya, playing important roles in RNA binding and turnover [24,25]. PPR domains contain successive helix-turn-helix motifs, with each motif containing ~35 amino acids, of which two are engaged to recognize a specific nucleotide [24]. The CZ domain connects the two arms (PPR and MN domains) in the V-shaped structure [26]. Lastly, the MN domain uses four aspartates to position at least two divalent cations (likely Mg^{2+} *in vivo*) to hydrolyze the scissile phosphodiester bond [10,27]. When the CZ domains in the crystal structures of *At*PRORP1 and *At*PRORP2 are superimposed, the orientations of the PPR domains differ by 35° and those of the MN domains by 45°. *At*PRORP2 displays a more open structure compared to *At*PRORP1 [4,20], with notable differences in the orientation of the two helices that make up the third PPR motif [20]. Recent mutagenesis and binding analyses of *At*PRORP1 and *At*PRORP2 [28] have revealed that the tight affinity of the PRORP-substrate complex is due to recognition of tRNA structure through ionic and non-ionic interactions, with the latter mediated by the PPR motifs.

Three studies have compared the ability of *At*PRORPs to bind and cleave pre-tRNAs [19,29,30]. All three *At*PRORPs coordinate Mg^{2+} using the pro-*Sp* oxygen of the scissile phosphodiester bond to promote cleavage, a difference from the RNase P RNP that coordinates the pro-*Rp* oxygen [29]. The catalytic parameters for binding and cleavage of two organellar and two nuclear *At* pre-tRNAs by the three PRORPs revealed a ~13-fold difference in k_{cat}/K_M and ~4-fold difference in binding affinity for any given pre-tRNA; despite these similarities, there were differences in the fidelity of processing with the highest miscleavage observed with *At*PRORP3 [19]. These findings, however, do not illuminate if the three *At*PRORPs occupy a distinctive phenotypic space because of their complementary functional repertoire.

Previous *in vitro* cleavage assays of *At*PRORPs have shown that *At*PRORP1 and *At*PRORP3 are capable of cleaving *Thermus thermophilus* pre-$tRNA^{Gly}$ at 37 °C, while *At*PRORP2 was inactive >30 °C [29]. Consistent with this observation, recent genetic complementation experiments showed that *At*PRORP2 could not support growth at 37 °C of *Escherichia coli* depleted of the RNase P RNP variant in sharp contrast to *At*PRORP1 and *At*PRORP3 [30]. These data indicate that *At*PRORP1 and *At*PRORP3 could support activity at slightly higher temperatures than *At*PRORP2, a surprising finding given the 88% primary sequence similarity between *At*PRORP2 and *At*PRORP3 [12,13]. One possible reason for a plant having multiple PRORPs is that the T_{opt} (temperature for optimal activity) of each isoform is fine-tuned to ensure tRNA 5′-maturation activity regardless of natural temperature fluxes. Although plants grow optimally over a range of temperatures (e.g., 4–25 °C for the *A. thaliana* Columbia ecotype), they exhibit some thermotolerance: for instance, even after 5 days at 36 °C, 50% of the *Arabidopsis* plants tested survived [31]. Therefore, we sought to better understand how the three *At*PRORPs fare over a broad range of temperatures in terms of stability and activity. Motivated by the idea that different physical attributes might engender payoffs under specific conditions, we examined the temperature–activity profiles for processing of select substrates by *At*PRORPs. Results from these studies, together with insights from all-atom, unbiased molecular dynamics (MD) simulations of *At*PRORP1 and *At*PRORP2, suggest payoffs that result from having three isoforms with distinct traits.

AtPRORPs Have Distinct Melting Temperatures

We determined the melting temperatures (T_m) of *At*PRORPs using differential scanning fluorimetry (DSF, Fig. S2; Table S1). We noted that *At*PRORP1 was the most stable among the three isoenzymes with a T_m of 48 ± 0 °C in 1 mM Mg^{2+}; based on a thermofluor melting curve, a T_m of 48.3 ± 0.1 °C was recently reported for *At*PRORP1 [28]. We found that *At*PRORP2 and *At*PRORP3 display T_m values of 34 ± 1 °C and 36 ± 1 °C, respectively, in 1 mM Mg^{2+}. Since large temperature fluctuations are common in the shoot in contrast to the root, *At*PRORP1 would be the preferred choice to support key organellar functions (respiration and photosynthesis) in the aerial parts of the plant. Indeed, the expression levels of *At*PRORPs in different parts of the plant (publicly available [32]) show that *At*PRORP1 is expressed at higher levels than *At*PRORP2 and *At*PRORP3 in organs exposed to the light, while the levels of *At*PRORP2 exceed *At*PRORP1 in the seed (Table S2).

*At*PRORPs Display Distinct Substrate-Dependent temperature–activity Profiles

To test the notion that the T_{opt} of each *At*PRORP isoform is fine-tuned to ensure tRNA biogenesis

under specific physiological conditions, we examined the temperature-dependent variation in the rates of cleavage of different substrates (Fig. 1). We first elaborate on the rationale for choosing a *Synechocystis* pre-tRNA^{Gln} and an *A. thaliana* chloroplast pre-tRNA^{Arg} [*At* chl–pre-tRNA^{Arg}(ACG)].

While the majority of tRNAs have a G_{+1}-C_{72} base pair (bp), some contain a U_{+1}-A_{72} bp; the correct RNase P cleavage (C_0) is between N_{-1} and N_{+1}. The *At* genome contains 659 tRNA genes: 4.2% have a U_{+1}-A_{72} and 3.3% have an A_{-1} and U_{+1}-A_{72}; the latter sequence is typified in *Synechocystis* (cyanobacterial) pre-tRNA^{Gln} (Fig. 1), a substrate that has been studied before by others and us [33–35] and one that we focused here for a few reasons. First, there is no information on how PRORPs process substrates (such as pre-tRNA^{Gln}) with a U_{+1}-A_{72}. Second, we already had available pre-tRNA^{Gln} mutant derivatives where the tRNA "elbow" has been weakened by extension of the D-stem [33], and sought to investigate the effect of such structural alterations on PRORP activity. Lastly, the *Synechocystis* tRNA^{Gln} is 90% identical to the *At* chloroplast counterpart making it a valid surrogate for studies of *At*PRORPs. Our second substrate of choice is *At* chl–pre-tRNA^{Arg}, which has an unusual acceptor stem with two unpaired bases (U_5:C_{69} and U_6:U_{68}; Fig. 1). Moreover, RNAi-based down-regulation of *At*PRORP1 led to impaired photosynthesis and accumulation of chl–pre-tRNA^{Arg}(ACG) and some other organellar pre-tRNAs [36]. Likewise, in the moss *Physcomitrella patens* (*Pp*), knockout lines of one of the organelle-targeted PRORPs led to a significantly decreased level of mature chl–tRNA^{Arg}(ACG) [15]. Only two nucleotides are different between *At* and *Pp* chl–pre-tRNA^{Arg} (ACG; which has a C_5 and U_{61}), with both containing two consecutive unpaired residues: U_5/C_5:C_{69} and U_6:U_{68}. These independent findings on the build-up of *At* or *Pp* chl–pre-tRNA^{Arg} [15,36], which confirm chl–pre-tRNA^{Arg} as a bona fide PRORP substrate despite its atypical structure, led to inclusion of *At* chl–pre-tRNA^{Arg}(ACG) in our studies.

Prior to initiating activity measurements, we used fluorescence polarization-based assays to determine the dissociation constants (K_D) for the binding of various substrates to *At*PRORPs. *At*PRORPs bind pre-tRNAs tested in this study with a wide range of K_D values (Table S3), although *At*PRORP1 exhibited the highest affinity. Overall, these K_D values helped guide the choice of enzyme concentrations for use in single-turnover assays. Moreover, we established that all three *At*PRORPs cleave pre-tRNA^{Gln} and its mutant derivatives at C_0, the correct cleavage site (Fig. S3); the fidelity of processing of pre-tRNA^{Arg}, however, was slightly variable, with *At*PRORP1 exhibiting predominantly correct cleavage (Fig. S4).

Using single-turnover studies, we obtained the k_{obs} values for processing of pre-tRNA^{Gln} from 4 to 37 °C by all three *At*PRORPs (Table S4). It was previously reported that k_{obs} values are comparable to k_{cat} determined under multiple-turnover conditions, a finding that is consistent with the rate-determining step being cleavage and not product release [19,27] (also, see Supplement for supporting data); therefore, experimentally determined k_{obs} values allow a comparison of the first-order rate constant for converting the enzyme-bound substrate to product by all three *At*PRORPs. Moreover, because K_D and K_M values are similar for various substrates processed by *At*PRORPs [19], k_{obs}/K_D could serve as a proxy for k_{cat}/K_M.

Based on the k_{obs} values that we determined, we calculated Q_{10} values (the fold-change in catalytic rate for every 10 °C increase; Table S5) to be 4, 3.5, and 3.4 for *At*PRORP1, *At*PRORP2, and *At*PRORP3, respectively. In general, the rates of an enzymatic reaction exhibit ~1.8-fold increase for an increase of 10 °C in assay temperature [37,38]. Eyring plots ($\ln k_{obs}/T$ *versus* $1/T$; not shown) of these data helped determine the enthalpy and entropy of activation (Table S5), while Arrhenius plots ($\ln k_{obs}$ *versus* $1/T$; Fig. S5) yielded activation energies of 24.1 ± 0.9, 20.9 ± 0.2 and 20.7 ± 0.8 kcal/mol for *At*PRORP1, *At*PRORP2 and *At*PRORP3, respectively. Collectively, these results suggest that organellar *At*PRORP1 requires additional activation energy relative to its nuclear cousins to perform phosphodiester hydrolysis.

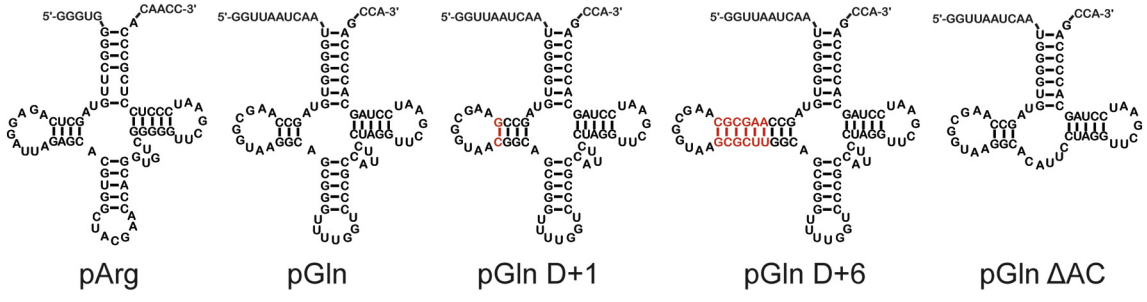

Fig. 1. Secondary structures of pre-tRNA substrates used for binding and cleavage assays with all three *At*PRORPs. Mutant derivatives (D + 1, D + 6, and ΔAC) of pre-tRNA^{Gln} have alterations to either the T-/D-tertiary contact or the anticodon stem; mutations are indicated in red. Abbreviations used: pArg, pre-tRNA^{Arg}; pGln, pre-tRNA^{Gln}.

Moreover, although a direct comparison is not possible given differences in assay pH and [Mg^{2+}], the E_a values for cleavage of pre-tRNA^{Gln} by *At*PRORPs are about two-fold higher compared to those reported for *E. coli* RNase P RNP (7.1–10.3 kcal/mol) [39,40]. The E_a for cleavage of the phosphodiester bond by ribozymes (13.5 kcal/mol) is intermediate to those of *E. coli* RNase P and *At*PRORPs [41,42].

To determine the T_{opt} of *At*PRORPs, we obtained the k_{obs} values for cleavage of pre-tRNA^{Gln} WT at six different temperatures between 4 and 45 °C, and additionally for four other substrates at 25, 37, and 42 °C (Figs. 2 and S6; Table S4). We discuss below the findings with pre-tRNA^{Gln} and other substrates. Based on the temperatures tested, the T_{opt} for cleavage of pre-tRNA^{Gln} is 37 °C for *At*PRORP2 and 42 °C for *At*PRORP1 and *At*PRORP3. Between 4 and 37 °C, there was a 100-fold increase in the rate of cleavage by *At*PRORP1 compared to a 60-fold increase with *At*PRORP2 and *At*PRORP3. There are distinct differences in the functional behavior of the isoenzymes above their respective T_{opt}. With *At*PRORP2, the k_{obs} value at 42 °C is two-fold lower compared to 37 °C and not measurable at 45 °C. The k_{obs} of *At*PRORP1 at 45 °C decreases by <20% compared to that determined at its T_{opt} (42 °C), but *At*PRORP3 decreased precipitously and showed only residual activity at 45 °C (product formation plateaued at 18% after a 1-h incubation and the k_{obs} could not be reliably calculated). To assess an approximate temperature ceiling for *At*PRORP1 function, we carried out an end-point measurement of cleavage activity and found only ~50% cleavage at 50 °C after a 6-min incubation compared to ~90% at 45 °C (data not shown).

We investigated if the trends observed with pre-tRNA^{Gln} are applicable to cleavage of select pre-tRNA^{Gln} mutant derivatives and pre-tRNA^{Arg} (Figs. 2 and S6; Table S4) at 25, 37, and 42 °C. Unlike the T_{opt} of 42 °C for pre-tRNA^{Gln}, *At*PRORP1 exhibits a T_{opt} of 37 °C for pre-tRNA$^{Gln(D+6)}$ and pre-tRNA^{Arg}, and ≥42 °C for pre-tRNA$^{Gln(D+1)}$ and pre-tRNA$^{Gln(\Delta AC)}$. For *At*PRORP2 and *At*PRORP3, the T_{opt} is 37 °C with pre-tRNA$^{Gln(D+1)}$, pre-tRNA$^{Gln(D+6)}$, pre-tRNA$^{Gln(\Delta AC)}$,

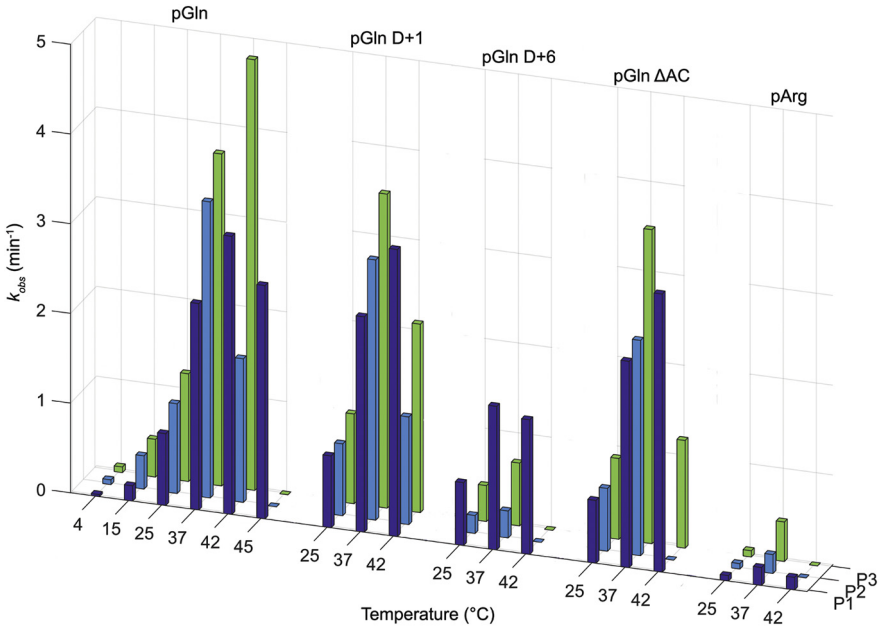

Fig. 2. Cleavage of pre-tRNAs by *At*PRORPs over a range of temperatures. Cleavage rates at the indicated temperatures represent the mean calculated from at least three independent experiments. The individual mean and standard deviation values are listed in Table S4 and summarized in a different format in Fig. S6. Approximately 40 nM 5′-[^{32}P]-labeled pre-tRNA was refolded as described [43]. Reactions were initiated by mixing an equal volume of *At*PRORP and pre-tRNA (both pre-incubated for 7 min at the assay temperature); assays were performed in 20 mM HEPES (pH 7.5), 1 mM $MgCl_2$, 150 mM NaCl, 4 mM DTT, and 5% (v/v) glycerol with a final concentration of 2 (or 6) μM *At*PRORP (Table S4). At each time point, a 5-μL aliquot was withdrawn from a 40-μL reaction and terminated using 10-μL stop solution [7 M urea, 20% (v/v) phenol, 0.2% (w/v) SDS, 10 mM EDTA, 0.05% (w/v) bromophenol blue, 0.05% (w/v) xylene cyanol]. Reaction contents were then separated using denaturing PAGE [8% or 25% (w/v) polyacrylamide, 7 M urea]. After visualization using the Typhoon Phosphorimager (GE Healthcare), the extent of cleavage was quantitated using ImageQuant 5.0 (GE Healthcare). Rates (k_{obs}) were calculated using KaleidaGraph 4.5 (Synergy) or JMP 11 (SAS Institute, Inc.) by fitting the data to $P_t = P_{max}(1 - e^{-k_{obs}t})$, where P_t is the product formed at time t. The values obtained from these two curve-fitting programs yielded similar, if not identical, values (not shown). Abbreviations used: P1, *At*PRORP1; P2, *At*PRORP2; P3, *At*PRORP3.

and pre-tRNA^{Arg}; however, the decrease above T_{opt} was always more pronounced for *At*PRORP2 than *At*PRORP3. The absence of a uniform trend in changes in k_{obs} for different pre-tRNAs indicates that T_{opt} values are substrate identity dependent, an unexpected finding.

There are some other inferences from these data. *At*PRORP1 is less sensitive to processing a pre-tRNA with perturbed D/T-loop interaction compared to *At*PRORP2/3, as evident from the activity–temperature profile with pre-tRNA$^{Gln(D+6)}$. Also, despite similar rates of processing of pre-tRNA$^{Gln(\Delta AC)}$ by all three PRORPs at 25 and 37 °C (Table S4), *At*PRORP1 binds this substrate with at least a ~13-fold lower K_D value at 25 °C (Table S3; see *Supplement*). Thus, based on k_{obs}/K_D (Tables S3 and S4), we conclude that the catalytic efficiency of *At*PRORP1 is 13-fold greater than that of *At*PRORP2 for cleavage of pre-tRNA$^{Gln(\Delta AC)}$ at 25 °C.

*At*PRORP2 could cleave all the substrates that we tested at 37 °C (and some even at 42 °C). These findings were unanticipated given a previous report documenting complete loss of *At*PRORP2 activity at 37 °C [29] as well as results from genetic complementation studies in *E. coli* and yeast where *At*PRORP2 was shown to be defective at 37 °C [30,44]. We recognize that the assay buffer conditions and the substrates used before are different from those employed in this work. To rule out buffer variations as a likely basis for differences with the earlier report [29], we assayed the pre-tRNA^{Gln}-processing activity of *At*PRORP2 at 37 °C in the buffer used before [29] and found robust cleavage similar to our buffer. Collectively, these results reinforce the idea that T_{opt} values are indeed substrate identity dependent, and that *At*PRORP2 can cleave at 37 °C a cyanobacterial pre-tRNA^{Gln} (this study) but not *T. thermophilus* pre-tRNA^{Gly} [29].

*At*PRORPs Have Distinct Dynamical Properties as Predicted by MD Simulations

Structures and simulations could help discern the molecular basis of protein and RNA catalysis [20,45–49], and prove instructive in unraveling substrate specificity and temperature–activity profiles of enzymes. Indeed, normal mode analyses (NMA) of the crystal structures of *At*PRORP1 and *At*PRORP2

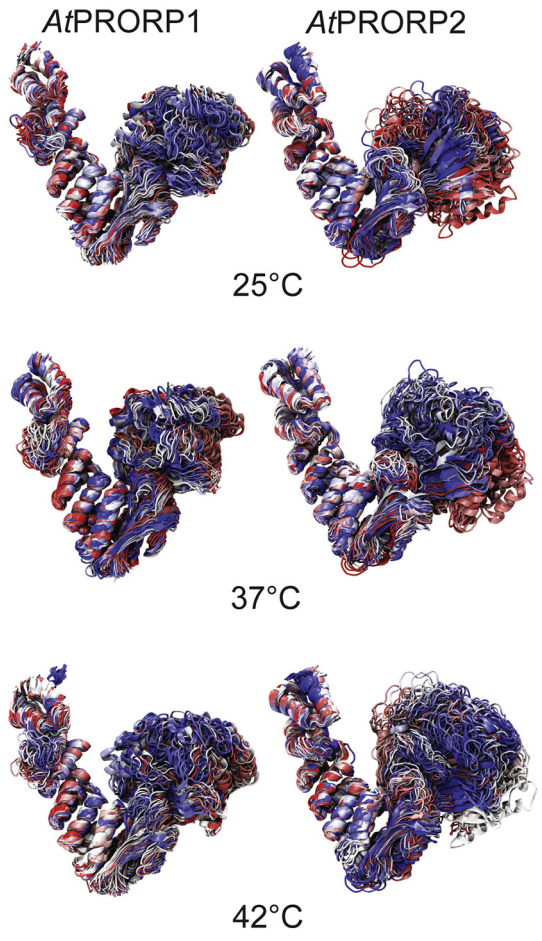

Fig. 3. Temperature-dependent dynamics of *At*PRORPs in MD simulations. Superposition of *At*PRORP1 (left panels) and *At*PRORP2 (right panels) conformations taken every 2 ns from 100-ns-long MD simulations performed at 25 °C (top), 37 °C (middle), or 42 °C (bottom). The PPR domain has been used as a reference for alignment of all conformations. Color ramp indicates time (red to white to blue). Two simulation systems were prepared using VMD [50]. The first one included the crystal structure of *At*PRORP1 solved at 1.95 Å (residues S95 to K570; PDB 4G24) [10], with two Mg^{2+} ions replacing crystallographically-resolved Mn^{2+} ions at the catalytic site, 330 crystallographic water molecules, and a single Zn^{2+} ion in the CZ domain. The second system included the crystal structure of *At*PRORP2 solved at 3.20 Å (N28 to S516 in chain A; PDB 5DIZ) [20] (see Supplement for additional details). The resulting simulation systems encompassed 133,230 atoms ($10.5 \times 11.7 \times 11.5$ nm^3) for *At*PRORP1 and 132,360 atoms ($11.7 \times 10.9 \times 11.1$ nm^3) for *At*PRORP2. Simulations (100 ns) were carried out using NAMD2.12 [51] and the CHARMM36 force field with the CMAP correction and the TIP3P water model [52–55]. Integration for the equations of motion was done using a 2-fs integration time step along with the SHAKE constraint algorithm for covalently bonded hydrogen atoms. Frames were saved every 2 ps, and van der Waals interactions were truncated using a cutoff of 12 Å with a switching function starting at 10 Å. The particle mesh Ewald method was used to compute long-range electrostatic interactions without any distance cutoff and with a grid density of >1 Å^{-3}. Temperature was controlled using Langevin dynamics with a damping coefficient of 0.1 ps^{-1}. The hybrid Nosé–Hoover Langevin piston method was used to control pressure (1 atm) using a 200-fs decay period and a 50-fs damping time constant. Each system was energy minimized and equilibrated in the constant number, pressure, and temperature ensemble (*NpT*) at 25, 37, or 42 °C.

indicated the presence of flexible hinges in the loop that connects the two helices of the third PPR motif (in the PPR domain) as well as between the CZ and MN domains in both proteins [20]. In another elegant study [49], NMA models and SAXS data were used to confirm conformational plasticity of *At*PRORP1 and *At*PRORP2, especially the rotation of the MN domain around the CZ domain/hinge. While these studies confirmed large-scale flexibility in solution and *in silico*, we sought atomistic insights into those motions in *At*PRORPs that might influence substrate recognition and T_{opt}. Therefore, we performed unbiased, all-atom 100-ns-long MD simulations at 25, 37 or 42 °C for *At*PRORP1 and *At*PRORP2 (the two isoforms for which a high-resolution structure is available), and monitored various structural properties throughout the resulting trajectories. The 100-ns-long simulations offer a first step to uncover the basis for functional differences between *At*PRORP1 and *At*PRORP2, primarily by examining if the conformational space sampled by these isoforms is different and temperature-dependent.

Visual inspection of the simulation trajectories revealed different behaviors for *At*PRORP1 and *At*PRORP2 (Fig. 3), with the latter exploring a larger number of conformations that deviated from the original conformation in the crystal structure. We quantitated this behavior by computing overall root mean square deviation (RMSD) and found that it was generally larger for *At*PRORP2 (2.2–8.8 Å, after first 10 ns) compared to *At*PRORP1 (1.6–5.8 Å) throughout the trajectories at 25, 37 or 42 °C (Fig. 4). Large RMSD values can reflect local deformations, relative motions of domains, or both. Therefore, we also

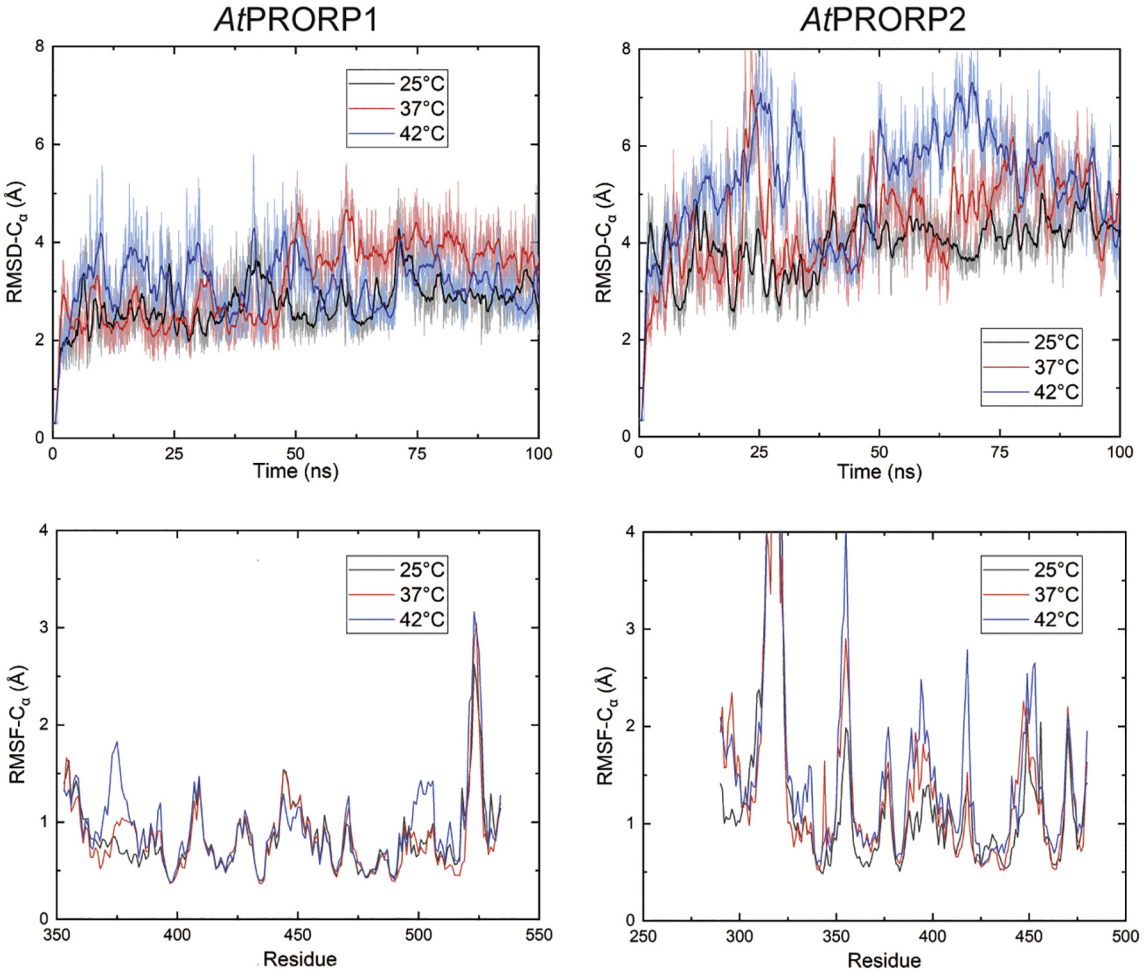

Fig. 4. Structural integrity of *At*PRORP1 and *At*PRORP2 in MD simulations. Top panels show RMSD computed using Cα-atom coordinates (RMSD-Cα) throughout the 100-ns-long MD simulations of *At*PRORP1 and *At*PRORP2, respectively. Initial models based on crystal structures (4G24 and 5DIZ) were used as references. Origin 2018 (OriginLab) was used to generate the smoothed curves (in darker color). Bottom panels show RMSF of Cα-atoms for residues in the catalytic MN domain computed without taking into account the first 10 ns of simulation. Results from simulations at 25, 37, or 42 °C are shown in black, red, or blue, respectively, in each panel. Additional details regarding data analyses are described in Supplementary Information.

computed RMSD per domain over entire trajectories and found low values (<2.5 Å) for the *At*PRORP1 MN and CZ domains, and medium values (< 3.5 Å) for the PPR domain at all three temperatures studied (data not shown). In contrast, at all temperatures investigated, RMSD values were low (<2.5 Å) for the *At*PRORP2 PPR domain and larger (> 2.5 Å) for the MN and CZ domains (data not shown). In addition, root mean square fluctuation (RMSF) values per residue, which reflect the extent of local dynamics, revealed a similar trend: the MN domain of *At*PRORP1 is generally less dynamic than the MN domain of *At*PRORP2 (Fig. 4). Together, these data suggest that (i) the CZ and MN domains in *At*PRORP1 are more rigid than in *At*PRORP2; (ii) the PPR domain in *At*PRORP1 is less rigid than in *At*PRORP2; and (iii) all domains are overall more mobile with respect to each other in *At*PRORP2.

Crystal structures of *At*PRORPs revealed that the aperture of the V-shape is different (Fig. 3). We quantitated this observation by computing the inter-domain angle between the PPR domain and the remainder of the protein (CZ plus MN domains) for the initial structures and for the conformations observed throughout our MD simulation trajectories (Figs. 3 and S7). Simulations predict that the inter-domain angle for *At*PRORP1 remains smaller than the *At*PRORP2 angle in solution (*in silico*) at 25, 37, and 42 °C over a 100-ns timescale. Simulations also revealed an initial and larger variation at 25 and 37 °C of the *At*PRORP2 aperture (compared to that of *At*PRORP1) that may reflect either release of strain from crystallographic contacts or intrinsic flexibility. At 37 °C (but not 42 °C), we also observed the formation of salt bridges in *At*PRORP1 (E246–R496) and *At*PRORP2 (E504–R443) after 50 ns, possibly accounting for decreased inter-domain angles (Fig. S8); mutagenesis studies are required to test the functional significance of these contacts at 37 °C. Overall, simulations predict that the inter-domain angle in *At*PRORP1 will be smaller than the one observed for *At*PRORP2, suggesting that this scenario is likely to hold in solution akin to that exemplified in their respective crystal structures. Such an inference is also consistent with their respective intrinsic flexibility, as evaluated in the NMA and SAXS modeling efforts [20,49]. Therefore, active substates may be diluted more rapidly for *At*PRORP2 than *At*PRORP1 as the temperature is increased.

Concluding Remarks

We have uncovered some physicochemical differences that suggest non-redundancy of three *At*PRORP isoforms in different physiological contexts. Our temperature–activity profiling showed that temperature ceilings for each PRORP isoform are substrate dependent. Overall, the T_{opt} trend is *At*PRORP1 > *At*PRORP3 > *At*PRORP2, which parallels the relative T_m values determined by DSF. However, such an inference masks the more nuanced picture that emerges from examining different substrates. For example, the T_m values of *At*PRORP2 and *At*PRORP3 at 34 ± 1 and 36 ± 1 °C, respectively, are lower than their T_{opt} of 37 and 42 °C for cleavage of pre-tRNA^{Gln} (i.e., $T_{opt} > T_m$). In contrast, *At*PRORP2 was reported to cleave a pre-tRNA^{Gly} at 28 °C but not 37 °C [29], despite a T_m of 34 °C; likewise, we show that *At*PRORP1 has a T_m of 48 °C but a T_{opt} of 42 °C with pre-tRNA^{Gln} (i.e., $T_m > T_{opt}$). In fact, a re-evaluation of the underpinnings for T_{opt} was prompted by instances where $T_m > T_{opt}$ for many enzymes [56-58].

The bell-shaped curves typically observed for activity *versus* temperature have often been attributed to Arrhenius behavior below T_{opt} and to protein denaturation above T_{opt}. However, alternative explanations have been sought given the examples of discord between T_{opt} and T_m [58,59]. The "equilibrium model" (Fig. S9) [60,61] postulates that enzymes toggle between active and inactive states in a rapid reversible transition (reflected in T_{opt}), with catalytic inactivation arising from local unfolding (reflected in T_m). An important corollary of the equilibrium model is that enzymes can reversibly lose activity due to the initial conformational sampling, and that increased stability is not the key to increased activity at high temperatures. The "macromolecular rate theory" [59,62] posits that the temperature dependence of enzyme-catalyzed reactions is independent of stability considerations and is rationalizable by the heat capacity difference ($\Delta C_p^{\ddagger}$) between the ground (ES) and transition (ES‡) states. We use these ideas to explain our observations on PRORPs, with implications for their biological roles.

First, the structure of *At*PRORP2 in solution appears more flexible than *At*PRORP1 [20,49], an inference supported by the RMSF values from our MD simulations (Figs. 3 and 4). Based on the equilibrium model, the comparatively ready loss of activity of *At*PRORP2 even at moderate temperatures is accounted for. Second, since curvature on either side of the T_{opt} is dictated by $\Delta C_p^{\ddagger}$ (based on the macromolecular rate theory), rate–temperature profiles need not be the same for different substrates tested with a given enzyme. Indeed, this is the case for all *At*PRORPs (Figs. 2 and S5). Third, the T_{opt} trend of *At*PRORP1 > *At*PRORP3 > *At*PRORP2 would predict a more rigid ground state for *At*PRORP1 and thus a less negative $\Delta C_p^{\ddagger}$. Given coincident k_{obs} values across the PRORPs, we rule out differences in the transition state as the basis for differences in $\Delta C_p^{\ddagger}$ among the PRORPs. While our results suggest that $\Delta C_p^{\ddagger}$ should be more negative for *At*PRORP2 relative to *At*PRORP1, additional experiments are required to confirm this expectation. Next, we consider the payoffs from a higher T_{opt} for *At*PRORP1 relative to its nuclear cousins.

The heat generated from operation of the electron transport chain was reported to increase the intramitochondrial temperature in human cells by ~10 °C compared to other cellular compartments [63]. If this increase also occurs in plant mitochondria, *At*PRORP1 would clearly be better equipped (among the three PRORPs) to respond to this temperature spike. Also, since large temperature fluxes are common in the shoot compared to the root, *At*PRORP1 would again be the preferred choice to support key organellar functions in the shoot, an expectation supported by publicly available transcriptomic data (Table S2).

While *At*PRORP1 is clearly a first among equals for organellar function, the use of its nuclear isoenzyme variants that display a lower T_{opt} seems intriguing at first glance. However, if lowering cytoplasmic translation is part of a high-temperature stress response, then *At*PRORP2 and *At*PRORP3 might be better candidates (than *AtPRORP1*) for regulatory control given that their lower T_{opt} and possibly a more negative $\Delta C_p^{\ddagger}$ will result in a sharp decline in activity above the T_{opt}. This disadvantage is counterbalanced by *At*PRORP2 and *At*PRORP3 enjoying a flexible ground state and a larger conformational ensemble (consistent with predictions from simulations and a more negative $\Delta C_p^{\ddagger}$) that allow a wider substrate suite, a decisive advantage if these nuclear PRORP variants are tasked with processing an array of pre-tRNAs and ncRNAs.

Our studies provide a glimpse of how choreographing conformational dynamics might modulate substrate specificity or temperature-dependent activity of *At*PRORPs. Differences in conformational sampling by each PRORP isoform might offer a mechanism to control their substrate repertoire at a given temperature. In this regard, the large number of native-like conformations sampled even at 25 °C, especially by *At*PRORP2, might ensure that a diverse ensemble is explored to facilitate cleavage of a broad substrate suite even if it is at the cost of occasional excursions into inactive conformations. A similar inference, which was drawn based on SAXS data, was used to support the idea that *At*PRORP2 might be more tolerant of tRNAs with long acceptor/T-stem stacks [49]. Thus, seemingly redundant isoforms might represent biological solutions to fulfill different functions on account of inherently different dynamics. It will be instructive to explore over long timescales the behavior of these multi-domain proteins, with and without bound substrates. Our simulations present testable ideas (e.g., importance of select salt bridges) to correlate structural flexibility and activity at elevated temperatures.

Another point of interest is the need for two nuclear PRORPs. Since knockdown of *At*PRORP2 or *At*PRORP3 had no deleterious consequences at 22 °C, they were postulated to be redundant [16]. Despite 88% similarity, *At*PRORP2 and *At*PRORP3 display significant binding affinity differences (e.g., pre-tRNA^{Gln}; Table S3). Thus, their substrate suites may differ and engender functional synergy in the nucleus. An additional testable possibility inspired by the rate–temperature profiles is that *At*PRORP2 might not fare well at elevated temperatures, and that *At*PRORP3 might offer a safety net under those conditions. Whether such non-redundant pleiotropic function is also the basis for two organellar PRORP variants in mosses [15], in contrast to the single isoform in land plants [13], merits investigation.

Acknowledgments

We thank members of the Gopalan laboratory for useful discussions that aided this work. We are indebted to Drs. Markos Koutmos (University of Michigan) and Carol Fierke (Texas A&M University) for providing expression plasmids encoding *At*PRORP2 and *At*PRORP3, respectively. We are also grateful to Dr. Edward Behrman (OSU) for providing fluorescein thiosemicarbazide and to Drs. Dmitri Kudryashov and Elena Kudryashova (OSU) for generously sharing reagents and equipment for DSF experiments. Simulations were performed at the Ohio Supercomputer Center (PAS1036) using the Owens supercomputer. This work was supported by the National Institutes of Health (GM-120582 to V.G.).

Appendix A. Supplementary data

Supplementary data to this article can be found online at https://doi.org/10.1016/j.jmb.2018.11.004.

Received 19 August 2018;
Received in revised form 22 October 2018;
Accepted 4 November 2018
Available online 8 November 2018

Keywords:
PRORP;
tRNA maturation;
substrate recognition;
temperature–activity profiles;
molecular dynamics

Abbreviations used:
PRORP, protein-only RNase P; MD, molecular dynamics; tRNA, transfer RNA; RNP, ribonucleoprotein; PPR, pentatricopeptide repeat domain; CZ, central bipartite zinc-binding domain; MN, metallonuclease domain.

References

[1] S. Altman, A view of RNase P, Mol. BioSyst. 3 (2007) 604–607.
[2] J.C. Ellis, J.W. Brown, The RNase P family, RNA Biol. 6 (2009) 362–369.

[3] O. Esakova, A.S. Krasilnikov, Of proteins and RNA: the RNase P/MRP family, RNA 16 (2010) 1725–1747.
[4] B.P. Klemm, N. Wu, Y. Chen, X. Liu, K.J. Kaitany, M.J. Howard, C.A. Fierke, The diversity of ribonuclease P: protein and RNA catalysts with analogous biological functions, Biomolecules 6 (2) (2016) 27, https://doi.org/10.3390/biom6020027.
[5] L.B. Lai, A. Vioque, L.A. Kirsebom, V. Gopalan, Unexpected diversity of RNase P, an ancient tRNA processing enzyme: challenges and prospects, FEBS Lett. 584 (2010) 287–296.
[6] W. Rossmanith, Of P and Z: mitochondrial tRNA processing enzymes, Biochim. Biophys. Acta 1819 (2012) 1017–1026.
[7] A.I. Nickel, N.B. Waber, M. Gossringer, M. Lechner, U. Linne, U. Toth, W. Rossmanith, R.K. Hartmann, Minimal and RNA-free RNase P in *Aquifex aeolicus*, Proc. Natl. Acad. Sci. U. S. A. 114 (2017) 11121–11126.
[8] J. Holzmann, P. Frank, E. Loffler, K.L. Bennett, C. Gerner, W. Rossmanith, RNase P without RNA: identification and functional reconstitution of the human mitochondrial tRNA processing enzyme, Cell 135 (2008) 462–474.
[9] M.J. Howard, X. Liu, W.H. Lim, B.P. Klemm, C.A. Fierke, M. Koutmos, D.R. Engelke, RNase P enzymes: divergent scaffolds for a conserved biological reaction, RNA Biol. 10 (2013) 909–914.
[10] M.J. Howard, W.H. Lim, C.A. Fierke, M. Koutmos, Mitochondrial ribonuclease P structure provides insight into the evolution of catalytic strategies for precursor-tRNA 5′ processing, Proc. Natl. Acad. Sci. U. S. A. 109 (2012) 16149–16154.
[11] N.J. Reiter, A. Osterman, A. Torres-Larios, K.K. Swinger, T. Pan, A. Mondragon, Structure of a bacterial ribonuclease P holoenzyme in complex with tRNA, Nature 468 (2010) 784–789.
[12] M. Lechner, W. Rossmanith, R.K. Hartmann, C. Tholken, B. Gutmann, P. Giege, A. Gobert, Distribution of ribonucleoprotein and protein-only RNase P in Eukarya, Mol. Biol. Evol. 32 (2015) 3186–3193.
[13] A. Gobert, B. Gutmann, A. Taschner, M. Gossringer, J. Holzmann, R.K. Hartmann, W. Rossmanith, P. Giege, A single *Arabidopsis* organellar protein has RNase P activity, Nat. Struct. Mol. Biol. 17 (2010) 740–744.
[14] A. Taschner, C. Weber, A. Buzet, R.K. Hartmann, A. Hartig, W. Rossmanith, Nuclear RNase P of *Trypanosoma brucei*: a single protein in place of the multicomponent RNA-protein complex, Cell Rep. 2 (2012) 19–25.
[15] C. Sugita, Y. Komura, K. Tanaka, K. Kometani, H. Satoh, M. Sugita, Molecular characterization of three PRORP proteins in the moss *Physcomitrella patens*: nuclear PRORP protein is not essential for moss viability, PLoS One 9 (2014), e108962.
[16] B. Gutmann, A. Gobert, P. Giege, PRORP proteins support RNase P activity in both organelles and the nucleus in *Arabidopsis*, Genes Dev. 26 (2012) 1022–1027.
[17] L.B. Lai, P. Bernal-Bayard, G. Mohannath, S.M. Lai, V. Gopalan, A. Vioque, A functional RNase P protein subunit of bacterial origin in some eukaryotes, Mol. Gen. Genomics. 286 (2011) 359–369.
[18] G. Bonnard, A. Gobert, M. Arrive, F. Pinker, T. Salinas-Giege, P. Giege, Transfer RNA maturation in *Chlamydomonas* mitochondria, chloroplast and the nucleus by a single RNase P protein, Plant J. 87 (2016) 270–280.
[19] M.J. Howard, A. Karasik, B.P. Klemm, C. Mei, A. Shanmuganathan, C.A. Fierke, M. Koutmos, Differential substrate recognition by isozymes of plant protein-only ribonuclease P, RNA 22 (2016) 782–792.
[20] A. Karasik, A. Shanmuganathan, M.J. Howard, C.A. Fierke, M. Koutmos, Nuclear protein-only ribonuclease P2 structure and biochemical characterization provide insight into the conserved properties of tRNA 5′ end processing enzymes, J. Mol. Biol. 428 (2016) 26–40.
[21] L. Reinhard, S. Sridhara, B.M. Hallberg, Structure of the nuclease subunit of human mitochondrial RNase P, Nucleic Acids Res. 43 (2015) 5664–5672.
[22] F. Li, X. Liu, W. Zhou, X. Yang, Y. Shen, Auto-inhibitory mechanism of the human mitochondrial RNase P protein complex, Sci. Rep. 5 (2015) 9878.
[23] D. Matelska, K. Steczkiewicz, K. Ginalski, Comprehensive classification of the PIN domain-like superfamily, Nucleic Acids Res. 45 (2017) 6995–7020.
[24] S. Manna, An overview of pentatricopeptide repeat proteins and their applications, Biochimie 113 (2015) 93–99.
[25] A. Filipovska, O. Rackham, Pentatricopeptide repeats: modular blocks for building RNA-binding proteins, RNA Biol. 10 (2013) 1426–1432.
[26] A. Gobert, F. Pinker, O. Fuchsbauer, B. Gutmann, R. Boutin, P. Roblin, C. Sauter, P. Giege, Structural insights into protein-only RNase P complexed with tRNA, Nat. Commun. 4 (2013) 1353.
[27] M.J. Howard, B.P. Klemm, C.A. Fierke, Mechanistic studies reveal similar catalytic strategies for phosphodiester bond hydrolysis by protein-only and RNA-dependent ribonuclease P, J. Biol. Chem. 290 (2015) 13454–13464.
[28] B.P. Klemm, A. Karasik, K.J. Kaitany, A. Shanmuganathan, M.J. Henley, A.Z. Thelen, A.J.L. Dewar, N.D. Jackson, M. Koutmos, C.A. Fierke, Molecular recognition of pre-tRNA by *Arabidopsis* protein-only ribonuclease P, RNA 23 (2017) 1860–1873.
[29] L.V. Pavlova, M. Gossringer, C. Weber, A. Buzet, W. Rossmanith, R.K. Hartmann, tRNA processing by protein-only versus RNA-based RNase P: kinetic analysis reveals mechanistic differences, Chembiochem 13 (2012) 2270–2276.
[30] M. Gossringer, M. Lechner, N. Brillante, C. Weber, W. Rossmanith, R.K. Hartmann, Protein-only RNase P function in *Escherichia coli*: viability, processing defects and differences between PRORP isoenzymes, Nucleic Acids Res. 45 (2017) 7441–7454.
[31] R.M. Warner, J.E. Erwin, Naturally occurring variation in high temperature induced floral bud abortion across *Arabidopsis thaliana* accessions, Plant Cell Environ. 28 (2005) 1255–1266.
[32] A.V. Klepikova, A.S. Kasianov, E.S. Gerasimov, M.D. Logacheva, A.A. Penin, A high resolution map of the *Arabidopsis thaliana* developmental transcriptome based on RNA-seq profiling, Plant J. 88 (2016) 1058–1070.
[33] W.Y. Chen, D. Singh, L.B. Lai, M.A. Stiffler, H.D. Lai, M.P. Foster, V. Gopalan, Fidelity of tRNA 5′-maturation: a possible basis for the functional dependence of archaeal and eukaryal RNase P on multiple protein cofactors, Nucleic Acids Res. 40 (2012) 4666–4680.
[34] V. Cognat, G. Pawlak, A.M. Duchene, M. Daujat, A. Gigant, T. Salinas, M. Michaud, B. Gutmann, P. Giege, A. Gobert, et al., PlantRNA, a database for tRNAs of photosynthetic eukaryotes, Nucleic Acids Res. 41 (2013) D273–D279.
[35] A. Pascual, A. Vioque, Substrate binding and catalysis by ribonuclease P from cyanobacteria and *Escherichia coli* are affected differently by the 3′ terminal CCA in tRNA precursors, Proc. Natl. Acad. Sci. U. S. A. 96 (1999) 6672–6677.
[36] W. Zhou, D. Karcher, A. Fischer, E. Maximova, D. Walther, R. Bock, Multiple RNA processing defects and impaired chloroplast function in plants deficient in the organellar protein-only RNase P enzyme, PLoS One 10 (2015), e0120533.

[37] G. Feller, Protein stability and enzyme activity at extreme biological temperatures, J. Phys. Condens. Matter 22 (2010), 323101.
[38] M. Elias, G. Wieczorek, S. Rosenne, D.S. Tawfik, The universality of enzymatic rate–temperature dependency, Trends Biochem. Sci. 39 (2014) 1–7.
[39] S. Cuzic, K.A. Heidemann, J. Wohnert, R.K. Hartmann, *Escherichia coli* RNase P RNA: substrate ribose modifications at G+1, but not nucleotide −1/+73 base pairing, affect the transition state for cleavage chemistry, J. Mol. Biol. 379 (2008) 1–8.
[40] A. Tallsjo, L.A. Kirsebom, Product release is a rate-limiting step during cleavage by the catalytic RNA subunit of *Escherichia coli* RNase P, Nucleic Acids Res. 21 (1993) 51–57.
[41] O.C. Uhlenbeck, A small catalytic oligoribonucleotide, Nature 328 (1987) 596–600.
[42] J.B. Thomson, D.M. Lilley, The influence of junction conformation on RNA cleavage by the hairpin ribozyme in its natural junction form, RNA 5 (1999) 180–187.
[43] T.H. Chen, A. Tanimoto, N. Shkriabai, M. Kvaratskhelia, V. Wysocki, V. Gopalan, Use of chemical modification and mass spectrometry to identify substrate-contacting sites in proteinaceous RNase P, a tRNA processing enzyme, Nucleic Acids Res. 44 (2016) 5344–5355.
[44] C. Weber, A. Hartig, R.K. Hartmann, W. Rossmanith, Playing RNase P evolution: swapping the RNA catalyst for a protein reveals functional uniformity of highly divergent enzyme forms, PLoS Genet. 10 (2014), e1004506.
[45] S. Hammes-Schiffer, Catalytic efficiency of enzymes: a theoretical analysis, Biochemistry 52 (2013) 2012–2020.
[46] M. Martick, T.S. Lee, D.M. York, W.G. Scott, Solvent structure and hammerhead ribozyme catalysis, Chem. Biol. 15 (2008) 332–342.
[47] Y. Shan, A. Arkhipov, E.T. Kim, A.C. Pan, D.E. Shaw, Transitions to catalytically inactive conformations in EGFR kinase, Proc. Natl. Acad. Sci. U. S. A. 110 (2013) 7270–7275.
[48] J. Villali, D. Kern, Choreographing an enzyme's dance, Curr. Opin. Chem. Biol. 14 (2010) 636–643.
[49] F. Pinker, C. Schelcher, P. Fernandez-Millan, A. Gobert, C. Birck, A. Thureau, P. Roblin, P. Giege, C. Sauter, Biophysical analysis of *Arabidopsis* protein-only RNase P alone and in complex with tRNA provides a refined model of tRNA binding, J. Biol. Chem. 292 (2017) 13904–13913.
[50] W. Humphrey, A. Dalke, K. Schulten, VMD: visual molecular dynamics, J. Mol. Graph. 14 (33–38) (1996) 27–38.
[51] J.C. Phillips, R. Braun, W. Wang, J. Gumbart, E. Tajkhorshid, E. Villa, C. Chipot, R.D. Skeel, L. Kale, K. Schulten, Scalable molecular dynamics with NAMD, J. Comput. Chem. 26 (2005) 1781–1802.
[52] A.D. MacKerell, D. Bashford, M. Bellott, R.L. Dunbrack, J.D. Evanseck, M.J. Field, S. Fischer, J. Gao, H. Guo, S. Ha, et al., All-atom empirical potential for molecular modeling and dynamics studies of proteins, J. Phys. Chem. B 102 (1998) 3586–3616.
[53] M. Buck, S. Bouguet-Bonnet, R.W. Pastor, A.D. MacKerell Jr., Importance of the CMAP correction to the CHARMM22 protein force field: dynamics of hen lysozyme, Biophys. J. 90 (2006) L36–L38.
[54] J. Huang, A.D. MacKerell Jr., CHARMM36 all-atom additive protein force field: validation based on comparison to NMR data, J. Comput. Chem. 34 (2013) 2135–2145.
[55] M. Karplus, G.A. Petsko, Molecular dynamics simulations in biology, Nature 347 (1990) 631–639.
[56] D. Georlette, B. Damien, V. Blaise, E. Depiereux, V.N. Uversky, C. Gerday, G. Feller, Structural and functional adaptations to extreme temperatures in psychrophilic, mesophilic, and thermophilic DNA ligases, J. Biol. Chem. 278 (2003) 37015–37023.
[57] S. D'Amico, J.C. Marx, C. Gerday, G. Feller, Activity-stability relationships in extremophilic enzymes, J. Biol. Chem. 278 (2003) 7891–7896.
[58] J. Clarke, K. Henrick, A.R. Fersht, Disulfide mutants of barnase. I: changes in stability and structure assessed by biophysical methods and X-ray crystallography, J. Mol. Biol. 253 (1995) 493–504.
[59] J.K. Hobbs, W. Jiao, A.D. Easter, E.J. Parker, L.A. Schipper, V.L. Arcus, Change in heat capacity for enzyme catalysis determines temperature dependence of enzyme catalyzed rates, ACS Chem. Biol. 8 (2013) 2388–2393.
[60] R.M. Daniel, M.J. Danson, A new understanding of how temperature affects the catalytic activity of enzymes, Trends Biochem. Sci. 35 (2010) 584–591.
[61] R.M. Daniel, M.J. Danson, Temperature and the catalytic activity of enzymes: a fresh understanding, FEBS Lett. 587 (2013) 2738–2743.
[62] V.L. Arcus, E.J. Prentice, J.K. Hobbs, A.J. Mulholland, M.W. Van der Kamp, C.R. Pudney, E.J. Parker, L.A. Schipper, On the temperature dependence of enzyme-catalyzed rates, Biochemistry 55 (2016) 1681–1688.
[63] D. Chretien, P. Benit, H.H. Ha, S. Keipert, R. El-Khoury, Y.T. Chang, M. Jastroch, H.T. Jacobs, P. Rustin, M. Rak, Mitochondria are physiologically maintained at close to 50 degrees C, PLoS Biol. 16 (2018), e2003992.